ARTICLE   **OPEN**

Check for updates

Shift current photovoltaic efficiency of 2D materials

Mikkel Ohm Sauer [ID][1,2,3 ✉], Alireza Taghizadeh[1,3,4], Urko Petralanda [ID][4,5], Martin Ovesen[1], Kristian Sommer Thygesen [ID][4,6], Thomas Olsen [ID][4], Horia Cornean[2] and Thomas Garm Pedersen [ID][1,3 ✉]

Shift current photovoltaic devices are potential candidates for future cheap, sustainable, and efficient electricity generation. In the present work, we calculate the solar-generated shift current and efficiencies in 326 different 2D materials obtained from the computational database C2DB. We apply, as metrics, the efficiencies of monolayer and multilayer samples. The monolayer efficiencies are generally found to be low, while the multilayer efficiencies of infinite stacks show great promise. Furthermore, the out-of-plane shift current response is considered, and material candidates for efficient out-of-plane shift current devices are identified. Among the screened materials, MXY Janus and MX_2 transition metal dichalchogenides (TMDs) constitute a prominent subset, with chromium based MXY Janus TMDs holding particular promise. Finally, in order to explain the band gap dependence of the PV efficiency, a simple gapped graphene model with a variable band gap is established and related to the calculated efficiencies.

INTRODUCTION

The photovoltaic (PV) effect, i.e. the direct conversion of solar energy to electricity, is a significant part of modern electricity generation. The majority of traditional PV devices are single p-n junction silicon cells, requiring hole- and electron-doped regions[1]. However, advances in materials technology have unveiled a new venue of PV materials, operating through shift currents (SCs), an example of "bulk photovoltaic effects"[2–23]. The SC is a second order nonlinear optical response observed in non-centrosymmetric semiconductors[5,24], generating a DC current. The name derives from the 'shift' of intracell coordinates of an excited electron due to its asymmetrical wave function, which drives the current[5]. The SC is a transport phenomenon intrinsic to the crystal. Thus, SC PVs do not require p-n junctions to separate optically generated electron-hole pairs. Consequently, the SC generation process is much faster than phonon emission[5], as opposed to current generation p-n junction PV devices, where carriers relax to the band edge with excess energy transferred into lattice excitation. Such losses restrict photovoltages in traditional p-n solar cells to values below the band gap, while SC devices can potentially generate above-gap photovoltages[5,16,17]. The band gap limit is a key component of the Shockley-Queisser efficiency limit, applying to traditional p-n junction cells[25]. As a result, this limit does not apply to SC devices[5,16,17].

In general, SCs are generated in non-centrosymmetric materials, which can be further divided into polar and non-polar categories[5,16]. Polar materials generate SCs in both polarized and unpolarized light[5], whereas non-polar materials require polarization[5]. Experimental SCs have been reported in a wide range of materials, including ferroelectrics[6–8], III/V quantum wells[9], organic crystals[10], and recently two-dimensional interfaces and materials[11–14,17,18,20,22]. Additionally, it has been shown that excitons play a significant role for second order effects in low-dimensional materials, increasing SCs by almost an order of magnitude at resonance[4,14]. The increase is significantly larger than the linear optical enhancement provided by excitons in the vicinity of the band gap[4,14,17]. This difference is attributed to the inter-exciton coupling present in second order optical responses, as demonstrated in a simple tight-binding-based Bethe-Salpeter model[4,26]. Research on SCs has yet to present any quantitative estimates of SC PV efficiencies from calculations or measurements of 2D materials[11–14,17,18,20,22]. Furthermore, previous works have had little focus on optimizing the band gap for SCs produced by solar radiation[4]. The lack of reliable estimates of efficiency and selection criteria constitute important challenges for the field of 2D SC devices.

In this work, we calculate and analyze the solar SC PV efficiencies, under idealized conditions, of 326 different dynamically stable, non-magnetic, non-centrosymmetric 2D semiconductors found in the computational database C2DB[27,28], 129 of which are non-polar, while 197 are polar, see Fig. 1a. This database contains material properties calculated from density functional theory. The calculation of PV efficiencies is based on the (1) SC spectra, (2) absorption spectra, (3) carrier mobilities, and (4) effective masses of each material, as described in the Methods section. An important distinction between traditional and SC PVs is that different parts of the solar spectrum may produce SCs of opposite sign. Such effects are not found in p-n junction PVs operating through absorption alone. As a consequence, it is advantageous to exclude part of the solar spectrum in SC devices. We therefore implement a low-pass filter, maximizing efficiencies by excluding photons above a certain energy threshold. The schematic in Fig. 1a illustrates PV power produced by SC J_{SC} generated in materials selected from C2DB[27,28] under illumination matching the reference air mass 1.5 spectrum[29]. As shown in the figure, the in-plane current is applied to assess efficiencies. This setup is presumably the most convenient for practical applications, requiring only end contacts. The out-of-plane response is briefly considered. However, collecting such currents would require separate top and bottom electrical contacts.

[1]Department of Materials and Production, Aalborg University, 9220 Aalborg Øst, Denmark. [2]Department of Mathematical Sciences, Aalborg University, 9220 Aalborg Øst, Denmark. [3]Center for Nanostructured Graphene (CNG), 9220 Aalborg Øst, Denmark. [4]Computational Atomic-scale Materials Design (CAMD), Department of Physics, Technical University of Denmark, 2800 Kgs. Lyngby, Denmark. [5]Department of Physics, University of the Basque Country (UPV/EHU), Apartado 644, Bilbao 48080, Spain. [6]Center for Nanostructured Graphene (CNG), 2800 Kgs. Lyngby, Denmark. ✉email: mikkelos@mp.aau.dk; tgp@mp.aau.dk
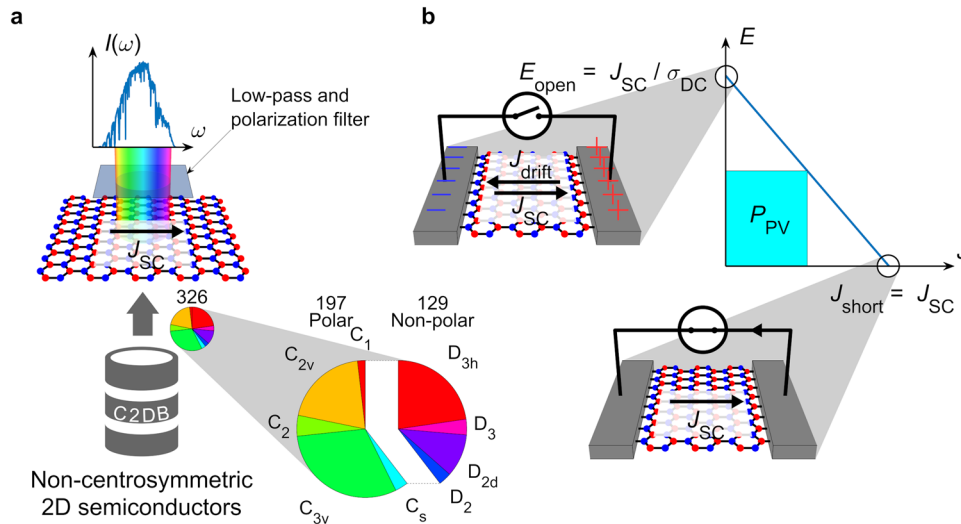
Fig. 1 Schematic of computational setup for shift current calculations. a Schematic view of SC power generation from 326 non-centrosymmetric 2D materials from C2DB and the reference air mass 1.5 spectrum[29], including a low-pass and polarization filter. The relative proportions of crystal symmetry groups are shown in the pie chart, divided into polar and non-polar materials. **b** E-J curve applied to calculate output power, with insets showing short circuit and open circuit scenarios. The area of the rectangle underneath the curve indicates the maximum PV power, P_{PV}.

RESULTS

PV efficiencies

In this section, PV efficiencies as well as in-plane and out-of-plane SCs will be presented. As shown in the Methods section, the PV efficiencies of a material are given by Eq. (11), which depends on (1) the effective mass, (2) the SC conductivity tensor, (3) the DC conductivity, and (4) the light absorption of the material, in addition to the spectral composition of incoming light. We apply C2DB effective masses, as well as 2D single-particle polarizabilities to obtain light absorptance[27]. Furthermore, the SC conductivity tensor is calculated in GPAW using an approach equivalent to the calculations of second-harmonic spectra in C2DB[28,30]. The specific parameters used for obtaining this SC tensor are a line width of $\Gamma = 50$ meV and a degeneracy tolerance of 10 meV, see ref. [30] for details. The SC conductivities, with all tensor elements, are available in C2DB (https://cmr.fysik.dtu.dk/c2db/c2db.html). The computational workflow has been applied to 326 non-centrosymmetric 2D semiconductors to obtain the PV efficiencies of these materials. Additionally, as mentioned previously, we apply a low-pass filter with a cutoff frequency maximizing efficiencies, since the sign of most SC conductivities feature positive and negative regions within the solar spectrum, reducing the overall current. Additionally, a filter reduces photo-generation rates G, leading to increased efficiency through the increased open circuit field, detailed in the Methods section. As shown below, this may place the optical filter cutoff even lower than expected from sign changes in the SC response. Such filters are found to increase efficiencies of some materials by a significant amount. As an example, an optimal low-pass filter increases the efficiency of CrSTe by a factor of approximately three.

Excitonic effects and self-energy corrections are not included in the calculations despite their potentially large impact on SC efficiencies[4]. Such effects are highly computationally demanding, making large scale workflows unfeasible at present[30]. The partial cancellation between excitonic and self-energy corrections[27] means that the simpler DFT-based onset of absorption as well as SC is expected to be reliable. This onset, along with geometric asymmetry, is an important indicator of performance. As a consequence, the ranking of materials based on DFT input is expected to be valid in the sense that promising candidates will remain so after excitonic and self-energy corrections. Finally, with

the exception of the efficiencies in Fig. 3, the carrier mobilities are assumed impurity-limited, as established in the Methods section.

Figure 2a, b compare the efficiencies of the most efficient materials with and without, respectively, a filter polarizing light along the x-direction. The calculated monolayer efficiencies are generally fairly low when compared to traditional p-n junction solar cells. The most efficient material is CrSTe with a polarization filter, having a PV efficiency $\eta_1^{(CrSTe)} \approx 0.28\%$. Calculations for y-polarized light have also been performed, however, for the majority of materials the efficiencies are practically equal and, thus, these results are not shown. This is especially true for materials with three- or four-fold symmetry for which they are exactly equal, which constitutes 219 of the 326 materials. Several of the highly efficient materials are MXY Janus structures, including the most efficient one, CrSTe. Additionally, 14 out of the 20 most efficient materials under polarized light contain chromium. The predicted efficiencies are highly sensitive to the assumed mobilities, with lower mobility enhancing open circuit voltage and, thereby, efficiency. As a consequence, high quality samples characterized by phonon-limited mobilities represent a worst-case scenario providing a lower bound for efficiencies. In Fig. 3a, b, phonon-limited results are shown for the twenty best material candidates. Note that these materials constitute an entirely different set than the ones in Fig. 2a, b. As expected, the results in Fig. 3 show a marked decrease in efficiency, with a peak efficiency $\approx 0.02\%$ found for the compound AsBrTe. These findings emphasize the critical role of mobilities for efficient SC devices.
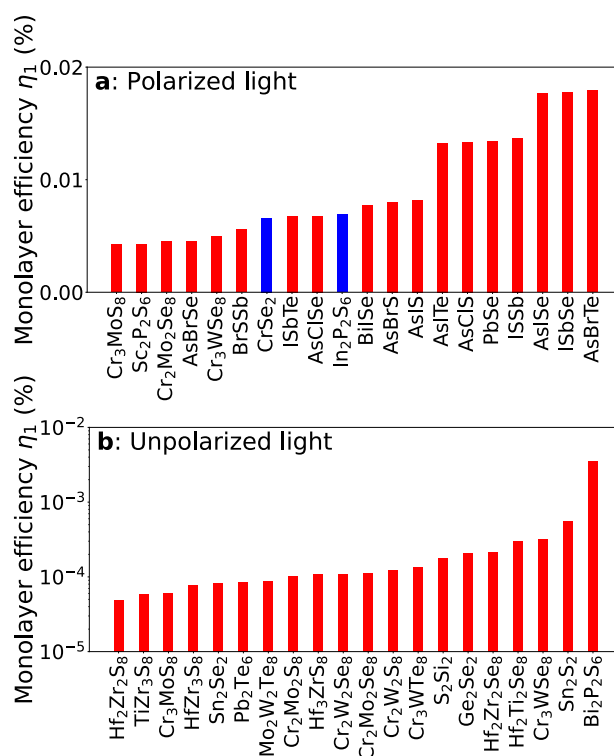
Examining polar and non-polar materials in Fig. 2, it is observed that adding a polarization filter increases the efficiencies of both classes. However, the majority of the highly efficient materials are polar. This connection between polarization, susceptibility, and SC has previously been studied, and found to be fairly complex[5,19]. In particular, these works found that an increase in the degree of polarization does not always imply an increase in SC[5,19]. One might expect the response of polar materials in the direction of spontaneous polarization to be superior compared to non-polar materials due to the inherent electric field that can help drive the current. This is, however, not what our data show, as the polar materials in Fig. 2a with the highest in-plane SC are polarized in the out-of-plane direction. In general, materials exhibit similar or smaller SC response in polar compared to non-polar directions,
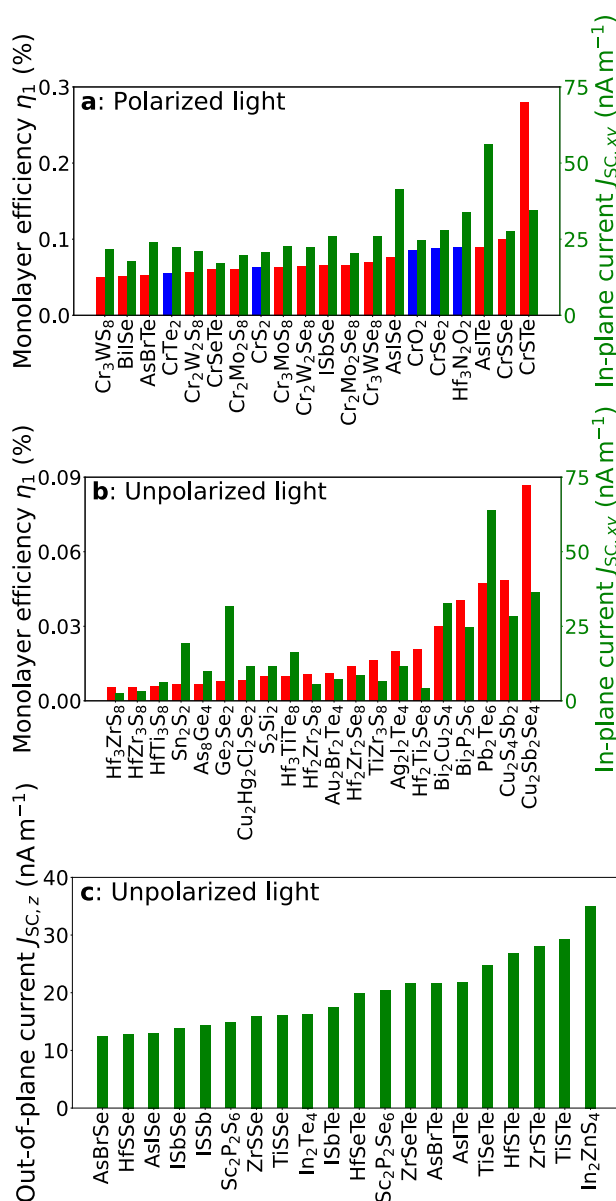
Fig. 2 Monolayer PV efficiencies with impurity-limited mobilities. **a**, **b** Monolayer PV efficiencies and in-plane SCs (green bars) of the twenty most efficient 2D materials, as calculated from Eq. (10), using parameters from C2DB and a standard solar spectrum, with **a** and without **b** polarization filter, respectively. The color of the bars in **a** indicate polar (red) and non-polar (blue) compounds. **c** Out-of-plane SC magnitude for the twenty materials with the highest response under unpolarized light.

Fig. 3 Monolayer PV efficiencies with phonon-limited mobilities. **a**, **b** Monolayer PV efficiencies of the twenty most efficient 2D materials, as calculated by Eq. (10) in the main document modified with the mobilities as calculated by the Takagi formulas (13) and (14), using parameters from C2DB and a standard solar spectrum, with and without a polarization filter. The color of the bars indicate polar (red) and non-polar (blue) compounds, respectively.

except for the fact that they typically have more non-vanishing tensor elements due to lower symmetry. This is in agreement with previous analyzes, which showed a complex relationship between the shift current response and spontaneous polarization[5,19]. The efficiencies under unpolarized light in Fig. 2b are significantly lower, and very few materials achieve noticeable efficiencies. The main reason is that only polar materials with an in-plane dipole can yield in-plane SCs without a polarization filter. Consequently, most materials are excluded, including many of the polar ones, such as all the MXY Janus structures, since these have only out-of-plane dipoles.

As argued above, efficiency depends on SC as well as absorption and carrier mobility. It is therefore important to explore the extent, to which SC alone correlates with efficiency. To

this end, we have included in-plane SCs in Fig. 2a, b, as well as out-of-plane SCs in Fig. 2c. In both cases, SCs are in units of nAm^{-1}, enabling simple comparison. We note, however, that the procedure providing the total current is different in the two cases. Thus, for in-plane SCs one multiplies $J_{SC,xy}$ by contact length. In contrast, the total out-of-plane current is found by dividing $J_{SC,z}$ by sample thickness and multiplying by sample area. This dimensional difference is exactly compensated by the fact that voltage is constant in the out-of-plane geometry, but varies linearly with distance between contacts in the in-plane case. Thus, in both cases, power is proportional to area, as expected. Examining Fig. 2a, b, we see that, generally, high efficiency correlates with high SC. Yet, a number of exceptions are noted. In particular, the most promising candidate CrSTe ranks third when ordered according to SC. Similarly, AsITe has the highest SC but ranks only third when considering efficiency. The explanation for this behavior is that CrSTe has a favorably low absorption and mobility for its SC response. Thus, the boost in open circuit voltage is sufficient to compensate for the lower SC. Conversely, AsITe features poor open circuit characteristics despite a very large SC response leading to an overall lower efficiency.

Comparing Fig. 2a, b and Fig. 2c we note that the largest out-of-plane SCs are similar in magnitude to the best in-plane ones, differing at most by a factor of two. This might potentially motivate further research into utilizing these materials by collecting out-of-plane currents. Obtaining an estimate for the efficiency of these SC materials, however, would require a different approach, as many of the material properties in the out-of-plane direction differ significantly from the in-plane ones, and are even more susceptible to effects of their surroundings.
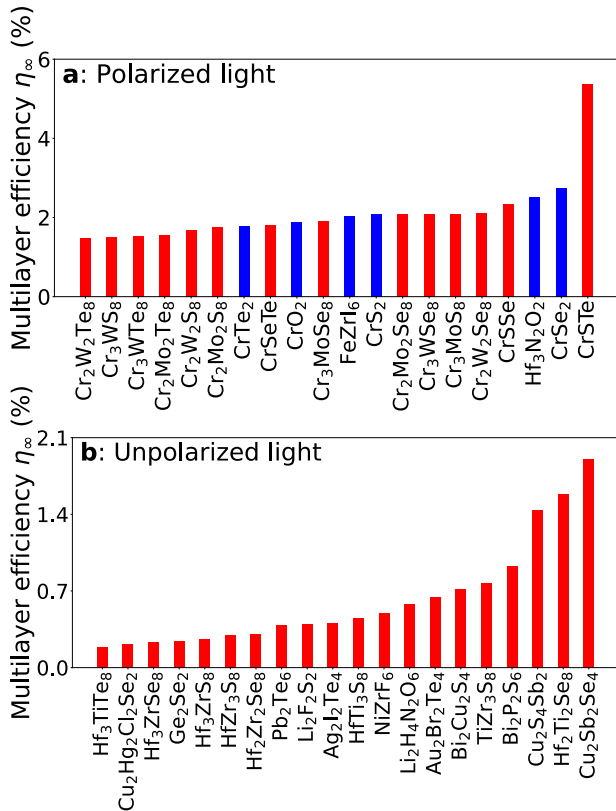
Fig. 4 Multilayer PV efficiencies. Multilayer PV efficiencies for the twenty most efficient 2D materials, using parameters from C2DB and a standard solar spectrum, with **a** and without **b** polarization filter. The bar colors in **a** indicate polar (red) and non-polar (blue) compounds, respectively.

Moreover, it is unclear how open circuit fields should be calculated in atomically thin out-of-plane geometries.

The multilayer PV efficiencies η_∞ (see Methods for details), shown in Fig. 4, exceed the monolayer efficiencies in Fig. 2 by one to two orders of magnitude. CrSTe still remains the most efficient material. However, several new extremely efficient materials appear, as exemplified by $FeZrI_6$ reaching $\eta_\infty \approx 2\%$. These high-efficiency candidates, which are absent in Fig. 2a, b, appear as a consequence of their very high Glass coefficient, i.e. ratio between SC and absorption. Thus, their monolayer response is poor but, by stacking many layers, the total response becomes significant. Physically, a large SC in a monolayer is typically accompanied by large absorption. However, in multilayer samples, even materials with low SC and absorption may fare well, as long as the ratio between the two is favorable. Finally, we note that the same mechanism applies to unpolarized light efficiencies, which are seen from Fig. 4b to increase by roughly the same factor as polarized ones.

Spectral response and data trends

We now investigate the spectral response of some of the most promising candidates in detail. Figure 5a, b show the shift current spectra for the most efficient polar and non-polar materials under polarized light, respectively. In addition, Fig. 5c, d illustrate the spectral response of the best polar material and the material with the highest out-of-plane shift current under unpolarized light. All spectra are calculated with a spectral broadening of 50 meV, leading to a non-zero SC tail below the band gap. The figures present only the yyy, yxx, and zyy tensor elements, as these are the relevant ones for normal incident light. For each material, the low-
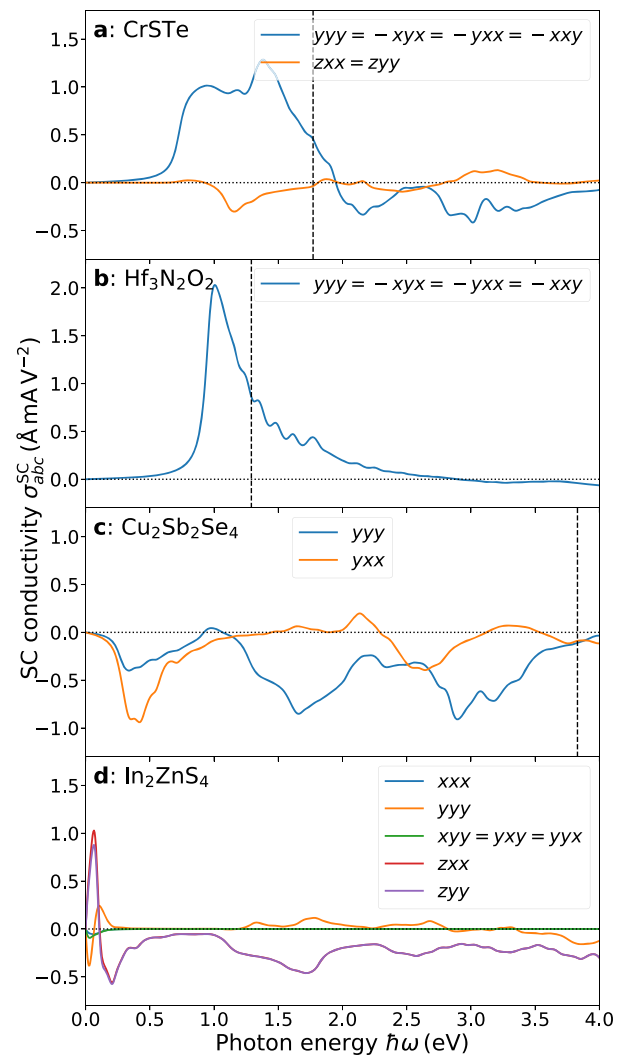

Fig. 5 Shift current spectra of selected materials. Shift current spectra of **a** CrSTe, **b** $Hf_3N_2O_2$, **c** $Cu_2Sb_2Se_4$, and **d** In_2ZnS_4, with a spectral broadening of 50 meV. Only tensor elements contributing to either efficiencies or out-of-plane shift current are shown. The vertical dashed lines show the low-pass filter cutoff.

pass cutoff is indicated by vertical dashed lines. None of the spectra overlap well with the solar spectrum, with two of the optimal low-pass filters removing more than half the irradiance, as shown by the cutoffs. Even so, these materials achieve the highest efficiencies due to a combination of very high SC tensor elements and low absorption. The seemingly non-optimal filter cutoffs discarding a portion of the SC response can be understood by considering the effect on photoinduced carriers reducing the open circuit field. Essentially, good performance can be achieved if the photo-generation rate G in Eq. (7) is sufficiently low, as follows from Eq. (10). As a consequence, it may be favorable to discard a larger part of the incoming spectrum even if this reduces the SC. This is particularly relevant if the omitted SC part is only a weak tail.

By compiling ab initio data for a wide range of materials, trends describing the impact of band gap E_g and composition can be deduced. The collection of 326 candidate materials includes both indirect and direct band gap compounds. However, we have ignored phonon-assisted processes that would add weak indirect transitions with an onset at the indirect band gap for the former class of compounds. Hence, all materials are treated as having
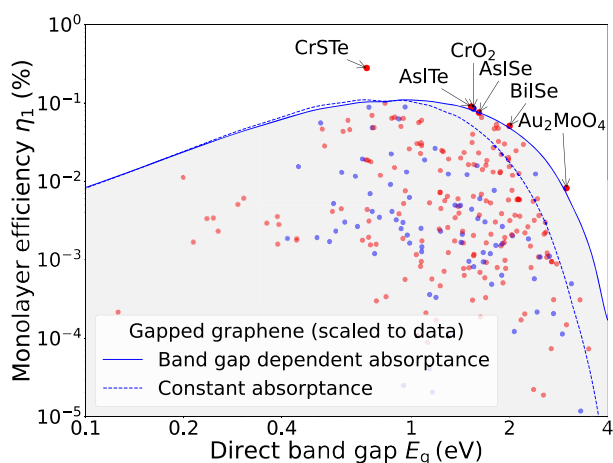
Fig. 6 Band gap dependence of PV efficiencies. Semilogarithmic plot of PV efficiencies vs. direct band gap. The curves represent the efficiency of gapped graphene as calculated by Eq. (17), including a finite line width of 50 meV. The color of the dots differentiate between polar (red) and non-polar (blue) compounds, respectively.

Fig. 7 Absorptance, SC conductivity, and efficiency of gapped graphene. a Unit cells of MXY Janus structure and gapped graphene. **b** PV efficiency vs. band gap for gapped graphene, as given by Eq. (17). Insets: Absorptance and SC conductivity spectra for gapped graphene, as given by Eqs. (15) and (16), respectively, with line width set to zero.

vanishing response to photon energies below the direct gap and, therefore, the direct band gap is the relevant indicator of performance.

In Fig. 6, monolayer efficiencies are plotted vs. direct band gap. There is clearly a significant scatter among the points. The frontier material CrSTe with $\eta_1^{(CrSTe)} \approx 0.28\%$ has a band gap of 0.67 eV. Yet, a broad optimum around direct band gaps of ~1 eV is noted. The fact that an optimal band gap exists is readily understood from the spectral match with the solar spectrum, similarly to usual p-n junction solar cells with an optimum around 1.35 eV[25]. Qualitatively, the spectral behavior of SC conductivity and absorption is similar, with vanishing response below the band gap and typically a peak immediately above the gap. Thus, photons in the energy range below the gap do not contribute to the response in neither p-n nor SC photovoltaics. This immediately explains the observed decrease in efficiency at high band gaps. The location of the optimum $E_g \sim 1$ eV is attributed to the peaked nature of $\sigma^{SC}(\omega)$ immediately above the band gap. A highly illustrative case in point is $Hf_3N_2O_2$ in Fig. 5b. In such cases, it is crucial that the solar spectrum maximum falls in the vicinity of the band gap, which explains the location of the optimum. In particular, lower band gaps imply reduced efficiency because $\sigma^{SC}(\omega)$ is typically small throughout the intense parts of the solar spectrum. An additional finding from Fig. 6 is a (weak) tendency for polar materials to be more efficient than non-polar ones, especially in the band gap range of 0.8–2 eV.

To rationalize these findings and guide searches for optimal materials, we seek to establish a much simpler analytical model capable of capturing the essential observations. To this end, we consider 'gapped graphene' as detailed in the Methods section and illustrated in Fig. 7a. Gapped graphene has hexagonal in-plane symmetry similar to TMDs and Janus structures and, as demonstrated by the insets in Fig. 7b, SC conductivity and absorption peaking just above the band gap. Applying these characteristic to the spectral integrals in Eq. (17) leads to band gap dependent efficiencies shown in the main panel of Fig. 7a and included in Fig. 6. It is clearly seen that the simplified model reproduces the optimum $E_g \sim 1$ eV.

A similar plot to Fig. 6 has been made by Tan et al., analyzing the integrated SC conductivity vs. band gap for 950 3D materials[23]. Here, the highest SC response is found in very low band gap materials, in agreement with our gapped graphene model detailed in the Methods section, where the SC conductivity scales inversely with the band gap. Their analysis does, however,
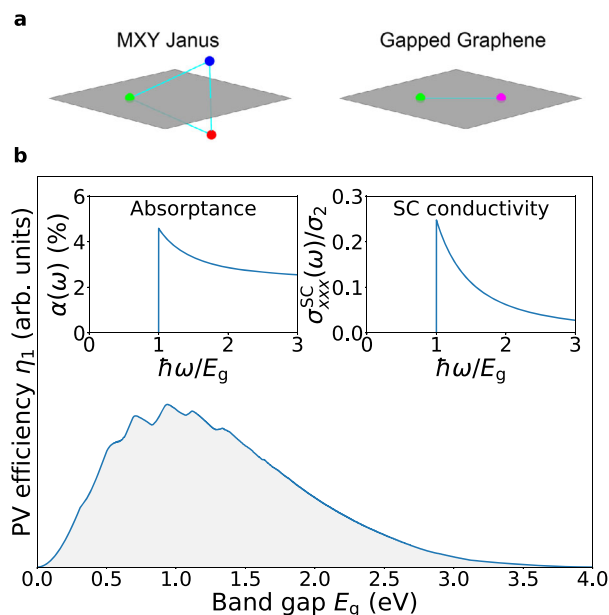
not include the solar spectrum in the integral, which is essential when calculating PV efficiency, as seen in Eq. (3). Thus, as previously stated, having a low band gap does not normally translate into high efficiency, since the solar intensity is very low in this energy range.

The simple gapped graphene model allows us to assess the impact of reduced absorption on the efficiency of high-gap materials. Thus, whereas traditional p-n solar cells require efficient absorption, SC photovoltaics may benefit from reduced absorption via the open circuit field, as noted above. To examine this hypothesis, we include in Fig. 6 the dashed curve obtained by assuming frequency-independent absorptance. In this manner, the increase in open circuit field resulting from high band gaps is artificially removed. As seen from the figure, the consequence is a significant reduction in efficiency in high-gap cases. This demonstrates that the optimum band gap region is, in fact, higher than would be expected based on SC alone.

We finally investigate the impact of chemical composition on the SC efficiencies. As is especially evident in Fig. 2a, a significant part of the most promising materials belongs to the TMD class, consisting of a metal and two vertically stacked atoms in a hexagonal lattice. This class is further subdivided into MX_2 TMDs and MXY Janus structures, where the vertically stacked atoms are non-identical. In Fig. 8, we analyze all (dynamically stable) combinations of 15 metals and 22 chalcogenide groups. The symmetric TMDs are represented by S_2, Se_2, Te_2, O_2 and I_2 dimers. In the plot, SC response and efficiency are shown as spot size, while color indicates direct band gap. Examining the trends in the results, it is observed that chromium compounds consistently rank among the best materials. Furthermore, as revealed by the color coding, Cr compounds feature band gaps on the plateau around the optimal band gap value predicted by the gapped graphene model. Consequently, this column of materials includes many promising candidates for SC PVs. It is interesting to note that, recently, Cr-based Janus TMDs have been identified as highly promising piezo-electric materials[31]. Similarly to second order nonlinear optics, piezo-electricity requires broken centrosymmetry
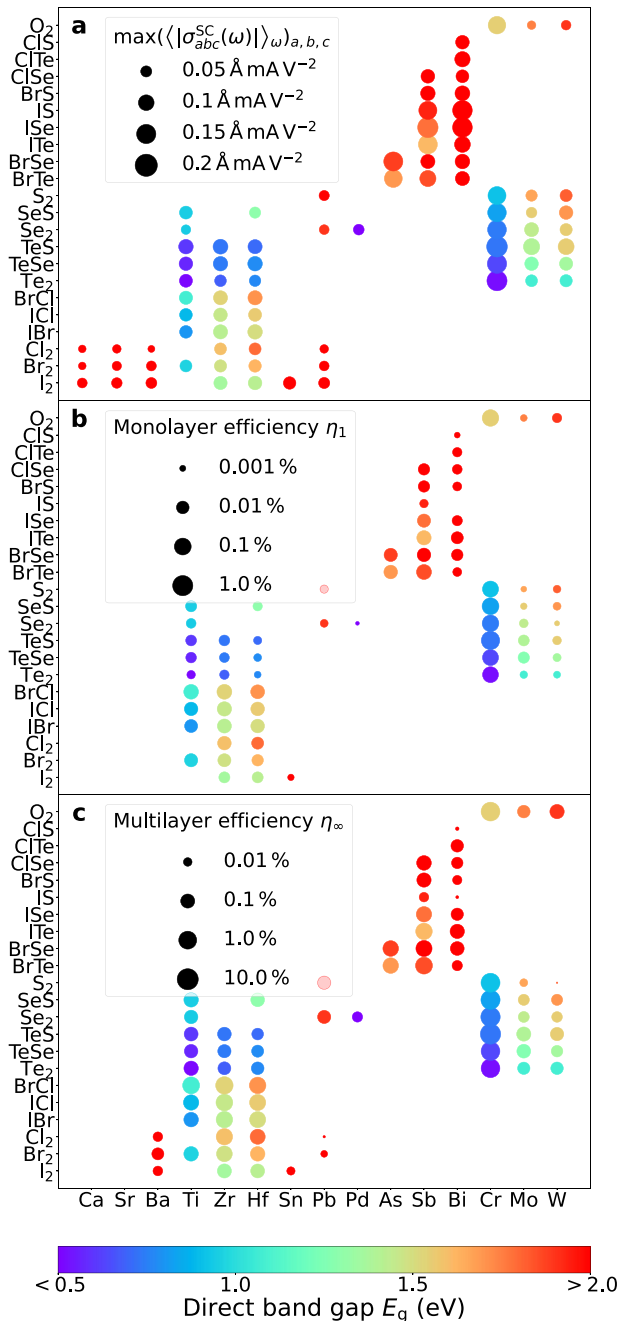
Fig. 8 Efficiency dependence of chemical composition. a Maximum SC tensor element magnitude averaged over frequency. Monolayer **b** and multilayer **c** PV efficiencies, for different TMDs of the MXY class. Horizontal and vertical axes show metal (M) and chalchogenide (XY) constituents, respectively.

implying a plausible connection between champion materials for both applications.

DISCUSSION

Shift current photovoltaic efficiencies of 326 distinct 2D materials present in the C2DB database have been calculated based on ab initio DFT-based shift current spectra. In addition, we demonstrate that linear optical absorption plays an important role for the material performance. We have formulated a rigorous approach relating efficiencies to microscopic quantities as well as experimental transport properties. In particular, we present results based on both theoretical phonon-limited mobilities as well as experimental impurity-scattering parameters. We find that the theoretical phonon-limited mobilities yield significantly lower efficiencies compared to impurity-limited mobilities. This is evident from Fig. 3, where the maximum efficiency under polarized and non-polarized light is reduced by an order of magnitude compared to the efficiencies in Fig. 2a, b. It is interesting that a different set of materials appear as the most efficient ones compared to the impurity-limited ranking in Fig. 2. This highlights the potential for exploiting and designing intrinsic mobilities in the search for promising SC photovoltaic materials[5]. Both in-plane and out-of-plane shift currents have been studied. Moreover, we find that efficiencies may be significantly improved by adding low-pass and polarization filters, optimized for each material. Finally, both monolayer and multilayer devices have been analyzed providing quantitative estimates of the gain achievable by stacking.

The multilayer efficiency η_∞ is closely related to an alternative measure of efficiency termed the internal efficiency, defined as $\eta_{int} = \frac{P_{pv}}{P_{abs}}$, where P_{abs} is the absorbed incident flux. For a single layer, the internal efficiency is significantly larger than the external one due to the relatively low absorptance of individual 2D monolayers, implying $P_{abs} \ll P_{inc}$. Consequently, the internal efficiency of a single layer is closely connected to that of an infinite stack, as both of them are proportional to the Glass coefficient (J_{SC}/P_{abs}) squared[7]. The multilayer efficiency η_∞ is, however, the physically more appealing of the two, because it refers to actual incident solar power rather than the absorbed fraction.

Among both mono- and multilayer devices with impurity-limited mobility, the highest efficiency is found in the Janus compound CrSTe. In fact, Cr-based compounds are generally highly promising featuring several champion material candidates. An important indicator for efficiency is the direct band gap, for which Cr-based compounds typically match the optimum around ~1 eV. The trade-off between shift current and absorption providing optimal performance has been elucidated in detail. We finally demonstrate that a simplified gapped graphene model explains several key findings including the band gap dependence of efficiency.

METHODS

Calculating PV efficiency

In this section, we will discuss the methodology applied to calculate PV efficiencies, while numerical results based on this approach are presented in the Results section. Two different PV efficiencies will be established: (1) the efficiency of a monolayer, and (2) the efficiency of an infinite stack of layers, ensuring complete absorption of the incident light. The external efficiency is defined as $\eta = \frac{P_{PV}}{P_{inc}}$ where $P_{inc} = \int_0^\infty I(\omega)d\omega$ is the total incident energy flux, with $I(\omega)$ being the irradiance of incoming light. In addition, P_{PV} is the electrical power extracted from the PV device.

Similarly to p-n junction PV devices, the power of a SC device can be related to its electric field-current (E-J) curve. As shown in Fig. 1b, this curve connects open and short circuit scenarios corresponding to infinite and vanishing external resistance, respectively. Additionally, the short circuit current $\mathbf{J}_{short}$ is equal to the shift current $\mathbf{J}_{SC}$. The maximum generated power is then the rectangle with the largest area drawn underneath the curve connecting open and short circuit end points. By introducing an E-J fill factor F, we get

$$P_{PV} = F\mathbf{J}_{short} \cdot \mathbf{E}_{open}. \tag{1}$$

Here, the dot product ensures that only the projection of the current onto the electric field yields any power. This is evident

from Fig. 1b, where any current flowing perpendicular to the electric field will produce a vanishing power. The E-J curve for a power source with a constant internal resistance, i.e. independent of the external load, is a linear curve between J_{short} and E_{open}, as shown in Fig. 1b, yielding a fill factor of $F = 1/4$[5].

The SC with a low-pass filter is given by

$$\mathbf{J}_{SC} = 2 \int_0^\infty \overleftrightarrow{\sigma}^{SC}(\omega) : \mathbf{E}(\omega)\mathbf{E}(-\omega)f(\omega)d\omega, \tag{2}$$

where $\overleftrightarrow{\sigma}^{SC}(\omega)$ is a third rank tensor describing the SC conductivity[30], $f(\omega)$ the low-pass filter function, the factor of two comes from the frequency permutation as derived by Sipe et al.[24], and $\mathbf{E}(\omega)$ is the incident electric field. Here, we assume an ideal low-pass filter, $f(\omega) = \Theta(\omega_{co} - \omega)$, with $\Theta(\omega)$ the Heaviside step function and ω_{co} the cutoff frequency. Placing the 2D sheet in the (x, y) plane, the irradiance at normal incidence can be related to the time-averaged electric fields squared as $I(\omega) = [\langle E_x^2(\omega)\rangle + \langle E_y^2(\omega)\rangle]/2Z_0$, where $Z_0 = \mu_0 c$ is the impedance of free space. Assuming unpolarized incident radiation $\langle E_x^2(\omega)\rangle = \langle E_y^2(\omega)\rangle$, and, moreover, $\langle E_x(\omega)E_x(-\omega)\rangle = \langle E_x^2(\omega)\rangle$. Thus, the shift current along direction a is

$$J_{SC,a} = 2Z_0 \int_0^\infty \sum_{b \in \{x,y\}} \sigma_{abb}^{SC}(\omega)I(\omega)f(\omega)d\omega, \tag{3}$$

where the sum is restricted to the diagonal in the last indices by considering two orthogonal projections of the unpolarized light separately. The off-diagonal contributions to the shift current of these two projections will cancel, leaving only the diagonal contributions[19]. As previously mentioned, non-polar materials will only generate current under polarized light[5]. Thus, in this case, we restrict the sum to either exclusively the x or y coordinate, corresponding to the effect of applying a polarization filter.

Next, as shown in Fig. 1b, in the open circuit case, J_{SC} is canceled by an equal and opposing drift current $J_{drift} = \sigma_{DC}E_{open}$, so that

$$E_{open} = J_{SC}/\sigma_{DC}. \tag{4}$$

Here, we assumed a diagonal DC conductivity σ_{DC}, which depends strongly on the material quality since it is proportional to the carrier mobility[4], i.e.

$$\sigma_{DC} = e(n\mu_e + p\mu_h), \tag{5}$$

where e is the elementary charge, n and p electron and hole density, respectively, and $\mu_{e/h}$ carrier mobilities of electrons/holes. We take the mobility tensors to be diagonal but possibly dependent on direction, as discussed below.

The mobility is notoriously dependent on environment and sample quality for 2D materials[32–35]. As is evident from Eqs. (4) and (5), a low mobility is favorable for SC devices due to an increased E_{open}. In ultra-clean, suspended materials one could apply the intrinsic (phonon limited) mobility, which can be estimated using the Takagi formula[36], Eq. (13). However, in experiments, 2D materials on substrates usually show significantly reduced mobilities compared to the intrinsic ones. This reduction is attributed to a number of different scattering mechanisms arising from the substrate itself and defects in the material. In particular, experiments show that, at room temperature, the primary source of scattering is Coulomb impurities near the semiconductor-dielectric interface[34]. Consequently, we will approximate the mobility based on experimental room temperature data for n-doped MoS$_2$. The mobility of MoS$_2$ on SiO$_2$ substrates has been found to be $\mu = 23$ cm^{2}V^{-1}s^{-1}[34,35], an order of magnitude lower than the intrinsic one. The electron mobility $\mu_e = e\langle\tau\rangle/m_e^*$ is proportional to the ratio between the energy weighted relaxation time $\langle\tau\rangle$ and effective electron mass m_e^*, with the former mostly sub- and superstrate dependent. Converting the measured mobility of MoS$_2$ into relaxation time using the

effective electron mass[27] $m_e^* = 0.53m_0$ yields $\langle\tau\rangle_{MoS_2} = 6.9 \cdot 10^{-15}$ s. Thus, assuming this value to be a reasonable general estimate, we will approximate the diagonal elements of the mobilities of other materials on similar substrates using

$$\mu_{e/h} = \frac{e\langle\tau\rangle_{MoS_2}}{m_{e/h}^*}, \tag{6}$$

where $m_{e/h}^*$ denotes electron/hole effective mass evaluated along the optical polarization direction. Here, the effective masses are reciprocally averaged over symmetric valleys, to handle multiple valance/conduction band maxima/minima. Hence, anisotropic effective masses lead to direction-dependent mobilities in materials with lower symmetry. To validate the applicability of a common relaxation time, we have compared calculated and measured mobilities of other prominent 2D materials. In this manner, we obtain mobilities for WSe$_2$ of $\mu_{e,WSe_2} \approx 27$ cm^{2}V^{-1}s^{-1} and $\mu_{h,WSe_2} \approx 35$ cm^{2}V^{-1}s^{-1}, close to experimentally measured values on SiO$_2$ of $\mu_{e/h,WSe_2} = 30$ cm^{2}V^{-1}s^{-1}[37]. Similarly, the measured hole mobility of few-layer BP on SiO$_2$ is $\mu_{h,BP} = 74$ cm^{2}V^{-1}s^{-1}[38], consistent with the mobility $\mu_{h,BP} = 81$ cm^{2}V^{-1}s^{-1} predicted by the effective mass of few-layer BP, $m_{h,BP}^* = 0.15m_0$[39].

In intrinsic semiconductors, charge neutrality implies $n = p$ and is maintained under illumination as electrons and holes are created simultaneously. Thus, assuming excitons dissociating instantaneously, the photoexcitation generation rate G is

$$G = \int_0^\infty a(\omega)\frac{I(\omega)}{\hbar\omega}f(\omega)d\omega, \tag{7}$$

where $a(\omega)$ is the absorptance of the material. This rate should be divided by a factor of 2, when considering a setup with a polarization filter. Assuming vanishing contributions from thermally excited carriers, the conductive electron density can now be determined from the density rate equation in steady state

$$\frac{dn}{dt} = G - \frac{n}{\tau_r} = 0 \Rightarrow n = G\tau_r, \tag{8}$$

where τ_r is the carrier lifetime before relaxing back to the ground state, i.e. the reciprocal of the recombination rate.

Combining these steps, we get the efficiency

$$\eta = \frac{F J_{SC}^2 m_{red}^*}{P_{inc} e^2 G \langle\tau\rangle_{MoS_2}\tau_r}, \tag{9}$$

where $m_{red}^* = m_e^* m_h^*/(m_e^* + m_h^*)$ is the reduced mass.

As with the mobilities, the carrier lifetime τ_r is subject to the same scattering mechanisms related to material quality, as well as sub- and superstrates. In lack of precise estimates of τ_r, the energy weighted relaxation time of MoS$_2$ provides a lower bound on this lifetime for all materials, yielding an upper bound on the efficiency. The relaxation time $\langle\tau\rangle_{MoS_2}$ is rather low compared to measured recombination lifetimes, that are on the scale of tens to thousands of fs, depending on the substrate, sample quality and contacts used[40–42]. However, the exact recombination lifetime in the presence of an electric field and metal contacts is difficult to estimate. Thus, we replace τ_r in Eq. (9), by the idealized lower bound $\tau_r = \langle\tau\rangle_{MoS_2}$, such that

$$\eta = \frac{F J_{SC}^2 m_{red}^*}{P_{inc} e^2 G \langle\tau\rangle_{MoS_2}^2}. \tag{10}$$

If the carrier lifetime is significantly larger than the idealized lower bound, this expression should be corrected by a factor of $\langle\tau\rangle_{MoS_2}/\tau_r$. Note that scaling $I(\omega)$ by a factor of C results in $J_{SC} \propto C$, $P_{inc} \propto C$, and $G \propto C$. Thus, the scaling factor cancels in the efficiency, meaning that efficiency is independent of the overall magnitude of the irradiance. This argument breaks down in the presence of ionizing defects, where the assumption of $n = G\tau$ is

invalid[4]. In this case, increasing P_{inc} improves the efficiency. These defects would optimally be passivated in SC PVs, since they reduce the overall efficiency[4,5]. The spectral composition of the irradiance does, however, play a significant role in the efficiency, due to a number of factors, the primary one being the spectral overlap with the SC susceptibility.

For an ideal stack of n layers, where each subsequent layer is exposed to the irradiance transmitted by the previous layers, the efficiency is

$$\eta_n = \frac{F\, m_{red}^*}{P_{inc}\, e^2\, \langle\tau\rangle_{MoS_2}^2} \sum_{m=1}^n \frac{J_{SC,m}^2}{G_m}, \tag{11}$$

where only $J_{SC,m}$ and G_m are layer-dependent quantities, determined by the irradiance reaching layer m

$$I_m(\omega) = (1 - a(\omega))^{m-1} I(\omega) f(\omega). \tag{12}$$

Clearly, for a single layer we insert $n = 1$ into Eq. (11) and obtain Eq. (10), as expected. In the opposite limit of an infinite stack, we insert $n = \infty$, resulting in the same expression of electric power as that of a single layer, except all occurrences of $I(\omega)$ are replaced by $I(\omega)/a(\omega)$. Note that we model multilayer samples as a stack of non-interacting layers, achieved by e.g. separating layers by a non-absorbing inert sheet, such as hBN. In this manner, the SC response of each individual layer is given by its monolayer value. Numerically, the ab initio absorptance below the direct band gap is very small, leading to potential numerical inaccuracies in the spectral integrals. To eliminate such errors, we add a small constant to the absorptance. This constant is taken as $2a_{FS}\Gamma/E_g$, with $a_{FS} \approx 1/137$ the fine-structure constant, $\Gamma = 50$ meV the line width, and E_g the direct band gap of the material. This expression is the DC absorptance of gapped graphene as given in Eq. (15).

Phonon-limited mobility

The intrinsic electron/hole mobility $\mu_{e/h}$, limited only by scattering on acoustic phonons, can be estimated using the deformation potential D by application of the Takagi formula[36], with in-plane diagonal elements

$$\mu_{e/h,aa} = \frac{e\hbar^3 S_{aa}}{k_B T m_{e/h,aa}^* m_{e/h,d}^* D_{e/h,a}^2}, \tag{13}$$

where S_{aa} is the diagonal elastic tensor elements, $m_{e/h,aa}^*$ the effective mass along direction a, and $m_{e/h,d}^* = \sqrt{m_{e/h,xx}^* m_{e/h,yy}^*}$. In anisotropic materials, the expression above should incorporate effects from the transverse direction[32]. As a consequence, the mobility must be multiplied by the factor[43]

$$\beta_{e/h} = \frac{\frac{5}{8} + \frac{3}{8}\frac{S_{bb}}{S_{aa}}}{\frac{9}{20} + \frac{7}{20}\frac{D_{e/h,b}}{D_{e/h,a}} + \frac{5}{20}\frac{D_{e/h,b}^2}{D_{e/h,a}^2}}, \tag{14}$$

where $b \neq a$ is the second in-plane direction.

Gapped graphene model

In the gapped graphene model, the actual 2D crystal is approximated by a staggered honeycomb lattice with two distinct sublattices, whose on-site energies are $\pm E_g/2$. Expanding sublattice coupling in the vicinity of the Dirac points to linear order in momentum yields a simple isotropic gapped Dirac model, which is sufficient to capture the linear optical response[44,45]. However, second-order nonlinearities require broken centrosymmetry and, therefore, so-called "trigonal warping" terms must be retained to compute shift currents[44,45]. Even including such terms, the model is sufficiently simple that closed-form analytical expressions of linear and nonlinear conductivities can be found. Thus, the absorptance and SC conductivity of gapped graphene in the

extended Dirac model are

$$a(\omega) = 2a_{FS} Im\left[\left(\frac{E_g^2}{\hbar^2\omega^2} + 1\right)\tanh^{-1}\left(\frac{\hbar\omega}{E_g}\right) - \frac{E_g}{\hbar\omega}\right], \tag{15}$$

$$\sigma_{xxx}^{SC}(\omega) = \frac{8\sigma_2\zeta_{TW}}{\pi} Im\left[\frac{E_g^2}{\hbar^2\omega^2}\tanh^{-1}\left(\frac{\hbar\omega}{E_g}\right) - \frac{E_g}{\hbar\omega}\right], \tag{16}$$

where $a_{FS} = e^2/4\pi\epsilon_0\hbar c$ is the fine-structure constant, a the lattice constant, $\zeta_{TW} = 1/8\sqrt{3}$ the trigonal-warping strength[46], and $\sigma_2 = e^3 a/4\hbar E_g$. As is evident, this model depends solely on one parameter, namely the band gap E_g, since the lattice constant a appears as a simple scaling factor in the SC. Assuming all other factors in the PV efficiency, Eq. (10), to be independent of E_g, the efficiency will be

$$\eta_1(E_g) \propto \frac{\left(\int_0^\infty \sigma_{xxx}^{SC}(\omega) I(\omega)\, d\omega\right)^2}{\int_0^\infty a(\omega) I(\omega)/\hbar\omega\, d\omega}. \tag{17}$$

This efficiency is shown in Fig. 7b, together with the absorptance and SC conductivity of gapped graphene. The efficiency is maximal near band gaps of approximately 1 eV. On either side of the optimum, efficiency is reduced due to poor spectral overlap between SC conductivity and solar spectrum. Note the extremely peaked nature of the SC conductivity at the band gap as shown in the inset of Fig. 7b. At higher band gaps, the reduced absorption also plays a role in the performance through the achieved open circuit field.

REFERENCES
1. Chapin, D. M., Fuller, C. S. & Pearson, G. L. A new silicon p-n junction photocell for converting solar radiation into electrical power. *J. Appl. Phys.* **25**, 676–677 (1954).
2. Sturman, B. & Fridkin, V. Photovoltaic and photo-refractive effects in non-centrosymmetric materials (Philadelphia, PA, Gordon and Breach Sci. Publ., 1992). https://books.google.dk/books?id=LfWRnGvIkecC.
3. Sturman, B. Ballistic and shift currents in the bulk photovoltaic effect theory. *Phys. Usp.* **63**, 407–411 (2020).
4. Chan, Y.-H., Qiu, D., Da Jornada, F. & Louie, S. Giant exciton-enhanced shift currents and direct current conduction with subbandgap photo excitations produced by many-electron interactions. *PNAS* **118**, e1906938118 (2021).
5. Tan, L. Z. et al. Shift current bulk photovoltaic effect in polar materials—hybrid and oxide perovskites and beyond. *Npj Comp. Mater.* **2**, 16026 (2016).
6. Auston, D. H., Glass, A. M. & Ballman, A. A. Optical rectification by impurities in polar crystals. *Phys. Rev. Lett.* **28**, 897–900 (1972).
7. Glass, A. M., von der Linde, D. & Negran, T. J. High-voltage bulk photovoltaic effect and the photorefractive process in linbo3. *Appl. Phys. Lett.* **25**, 233–235 (1974).
8. Somma, C., Reimann, K., Flytzanis, C., Elsaesser, T. & Woerner, M. High-field terahertz bulk photovoltaic effect in lithium niobate. *Phys. Rev. Lett.* **112**, 146602 (2014).
9. Bieler, M., Pierz, K., Siegner, U. & Dawson, P. Shift currents from symmetry reduction and coulomb effects in (110)-orientated GaAs/al0.3ga0.7As quantum wells. *Phys. Rev. B* **76**, 161304 (2007).
10. Ogden, T. R. & Gookin, D. M. Bulk photovoltaic effect in polyvinylidene fluoride. *Appl. Phys. Lett.* **45**, 995–997 (1984).

11. Nakamura, M. et al. Spontaneous polarization and bulk photovoltaic effect driven by polar discontinuity in lafeo₃/srtio₃ heterojunctions. *Phys. Rev. Lett.* **116**, 156801 (2016).

12. Kaner, N. T. et al. Enhanced shift currents in monolayer 2d ges and sns by strain-induced band gap engineering. *ACS Omega* **5**, 17207–17214 (2020).

13. Morimoto, T., Nakamura, M., Kawasaki, M. & Nagaosa, N. Current-voltage characteristic and shot noise of shift current photovoltaics. *Phys. Rev. Lett.* **121**, 267401 (2018).

14. Fei, R., Tan, L. Z. & Rappe, A. M. Shift-current bulk photovoltaic effect influenced by quasiparticle and exciton. *Phys. Rev. B* **101**, 045104 (2020).

15. Nakamura, M. et al. Shift current photovoltaic effect in a ferroelectric charge-transfer complex. *Nat. Commun.* **8**, 281 (2017).

16. Dai, Z. & Rappe, A. M. Recent progress in the theory of bulk photovoltaic effect. *Chem. Phys. Rev.* **4**, 011303 (2023).

17. Dai, Z. & Rappe, A. M. First-principles calculation of ballistic current from electron-hole interaction. *Phys. Rev. B* **104**, 235203 (2021).

18. Sheng, Y. et al. Bulk photovoltaic effect in hexagonal lumno₃ single crystals. *Phys. Rev. B* **104**, 184116 (2021).

19. Young, S. M. & Rappe, A. M. First principles calculation of the shift current photovoltaic effect in ferroelectrics. *Phys. Rev. Lett.* **109**, 116601 (2012).

20. Osterhoudt, G. et al. Colossal mid-infrared bulk photovoltaic effect in a type-i weyl semimetal. *Nat. Mater.* **18**, 471 (2019).

21. Brehm, J. A., Young, S. M., Zheng, F. & Rappe, A. M. First-principles calculation of the bulk photovoltaic effect in the polar compounds liass2, liasse2, and naasse2. *J. Chem. Phys.* **141**, 204704 (2014).

22. Rangel, T. et al. Large bulk photovoltaic effect and spontaneous polarization of single-layer monochalcogenides. *Phys. Rev. Lett.* **119**, 067402 (2017).

23. Tan, L. Z. & Rappe, A. M. Upper limit on shift current generation in extended systems. *Phys. Rev. B* **100**, 085102 (2019).

24. Sipe, J. E. & Shkrebtii, A. I. Second-order optical response in semiconductors. *Phys. Rev. B* **61**, 5337–5352 (2000).

25. Shockley, W. & Queisser, H. J. Detailed balance limit of efficiency of p-n junction solar cells. *J. Appl. Phys.* **32**, 510–519 (1961).

26. Pedersen, T. G. Intraband effects in excitonic second-harmonic generation. *Phys. Rev. B* **92**, 235432 (2015).

27. Haastrup, S. et al. The computational 2D materials database: high-throughput modeling and discovery of atomically thin crystals. *2D Mater.* **5**, 042002 (2018).

28. Gjerding, M. N. et al. Recent progress of the computational 2D materials database (C2DB). *2D Mater.* **8**, 044002 (2021).

29. ASTM G173-03(2020), *Standard tables for reference solar spectral irradiances: direct normal and hemispherical on 37° tilted surface* (ASTM International, West Conshohocken, PA, 2020).

30. Taghizadeh, A., Thygesen, K. S. & Pedersen, T. G. Two-dimensional materials with giant optical nonlinearities near the theoretical upper limit. *ACS Nano* **15**, 7155–7167 (2021).

31. Chen, S. et al. Large tunable rashba spin splitting and piezoelectric response in janus chromium dichalcogenide monolayers. *Phys. Rev. B* **106**, 115307 (2022).

32. Mir, S., Yadav, V. & Singh, J. Recent advances in the carrier mobility of two-dimensional materials: A theoretical perspective. *ACS Omega* **5**, 14203–14211 (2020).

33. Ahmed, S. & Yi, J. Two-dimensional transition metal dichalcogenides and their charge carrier mobilities in field-effect transistors. *Nanomicro Lett.* **9**, 50 (2017).

34. Yu, Z. et al. Analyzing the carrier mobility in transition-metal dichalcogenide mos2 field-effect transistors. *Adv. Funct. Mater.* **27**, 1604093 (2017).

35. Yu, Z. et al. Towards intrinsic charge transport in monolayer molybdenum disulfide by defect and interface engineering. *Nat. Commun.* **5**, 5290 (2014).

36. Takagi, S., Toriumi, A., Iwase, M. & Tango, H. On the universality of inversion layer mobility in si mosfet's: Part i-effects of substrate impurity concentration. *IEEE Trans. Electron Devices* **41**, 2357–2362 (1994).

37. Allain, A. & Kis, A. Electron and hole mobilities in single-layer wse2. *ACS Nano* **8**, 7180–7185 (2014).

38. Wood, J. D. et al. Effective passivation of exfoliated black phosphorus transistors against ambient degradation. *Nano Lett.* **14**, 6964–6970 (2014).

39. Qiao, J., Kong, X., Hu, Z.-X., Yang, F. & Ji, W. High-mobility transport anisotropy and linear dichroism in few-layer black phosphorus. *Nat. Commun.* **5**, 4475 (2014).

40. Grubišić Čabo, A. et al. Observation of ultrafast free carrier dynamics in single layer mos2. *Nano Lett.* **15**, 5883–5887 (2015).

41. Parzinger, E., Hetzl, M., Wurstbauer, U. & Holleitner, A. W. Contact morphology and revisited photocurrent dynamics in monolayer mos2. *Npj 2D Mater. Appl.* **1**, 40 (2017).

42. Bussolotti, F., Yang, J., Kawai, H., Chee, J. Y. & Goh, K. E. J. Influence of many-body effects on hole quasiparticle dynamics in a ws₂ monolayer. *Phys. Rev. B* **103**, 045412 (2021).

43. Zhou, M., Chen, X., Li, M. & Du, A. Widely tunable and anisotropic charge carrier mobility in monolayer tin(ii) selenide using biaxial strain: a first-principles study. *J. Mater. Chem. C.* **5**, 1247–1254 (2017).

44. Pedersen, T. G. Linear and nonlinear optical and spin-optical response of gapped and proximitized graphene. *Phys. Rev. B* **98**, 165425 (2018).

45. Hipolito, F., Pedersen, T. G. & Pereira, V. M. Nonlinear photocurrents in two-dimensional systems based on graphene and boron nitride. *Phys. Rev. B* **94**, 045434 (2016).

46. Taghizadeh, A. & Pedersen, T. G. Nonlinear optical selection rules of excitons in monolayer transition metal dichalcogenides. *Phys. Rev. B* **99**, 235433 (2019).

47. Mortensen, J. J., Hansen, L. B. & Jacobsen, K. W. Real-space grid implementation of the projector augmented wave method. *Phys. Rev. B* **71**, 035109 (2005).

48. Enkovaara, J. et al. Electronic structure calculations with GPAW: a real-space implementation of the projector augmented-wave method. *J. Phys. Condens. Matter* **22**, 253202 (2010).

ACKNOWLEDGEMENTS

AUTHOR CONTRIBUTIONS

M.O.S. developed the efficiency model, performed efficiency calculation and wrote the initial draft. A.T., U.P., K.S.T., and T.O. developed the DFT code and performed DFT calculations. M.O. contributed to developing the model. T.G.P. supervised the project. All authors contributed to the manuscript.

COMPETING INTERESTS

The authors declare no competing interests.

ADDITIONAL INFORMATION

Correspondence and requests for materials should be addressed to Mikkel Ohm Sauer or Thomas Garm Pedersen.

Reprints and permission information is available at http://www.nature.com/reprints

Publisher's note Springer Nature remains neutral with regard to jurisdictional claims in published maps and institutional affiliations.